Role of anisotropy in the elastoplastic response of a polygonal packing

F. Alonso-Marroquín*
ICP, University of Stuttgart, Pfaffenwaldring 27, 70569 Stuttgart, Germany and National Technical University of Athens, 5 Heroes of Polytechnion, 15773 Athens, Greece

S. Luding†
Particle Technology, DelftChemTech, TU Delft, Julianalaan 136, 2628 BL Delft, The Netherlands

H. J. Herrmann‡
ICP, University of Stuttgart, Pfaffenwaldring 27, 70569 Stuttgart, Germany

I. Vardoulakis§
National Technical University of Athens, 5 Heroes of Polytechnion, 15773 Athens, Greece
(Received 1 March 2004; revised manuscript received 27 December 2004; published 16 May 2005)

We study the effect of the anisotropy induced by loading on the elastoplastic response of a two dimensional discrete element model granular material. The anisotropy of the contact network leads to a breakdown of the linear isotropic elasticity. We report on a linear dependence of the Young moduli and Poisson ratios on the fabric coefficients, measuring the anisotropy of the contact network. The resulting nonassociated plastic flow rule and the linear relationship between dilatancy and stress ratio are discussed in terms of several existing models. We propose a paradigm for understanding soil plasticity, based on the correlation between the plastic flow rule and the induced anisotropy on the subnetwork of sliding contacts.

DOI: 10.1103/PhysRevE.71.051304 PACS number(s): 45.70.Cc, 83.10.Gr, 61.43.Bn, 83.80.Nb

I. INTRODUCTION

Granular materials exhibit a range of behavior that has attracted the attention of physicists, mathematicians, and engineers from Coulomb, Faraday and Reynolds in the late 18th century, to several interdisciplinary research groups in the earlier 21st, trying to improve the handing of agricultural an pharmaceutical products, and to understand the material behavior of construction materials such as ballast, concrete, marble, etc. It is therefore surprising that perhaps the simplest question of dilatancy remains unanswered even now. In the simplest case of noncohesive granular materials, the conventional elastoplastic models interpret the dilatancy using the hypothesis of the existence of a finite domain in stress space where only elastic deformations are possible [1]. Astonishingly, a large amount of experimental evidence suggests that the purely elastic regime in such materials is vanishingly small [2]. This proves that the introduction of such an elastic regime in the continuous description may be as unnecessary as unsuitable. For this reason sand is sometimes mathematically described by using a rigid-plastic limit which is called the *psammic limit*, where dilatancy is seen as an internal constraint [3,4].

Several recent investigations on granular materials at grain scale have provided another context for understanding the mechanical response of granular assemblies [5–7]. Even in the absence of strong spatial disorder of the grains, static assemblies show that the stress is transmitted through an heterogeneous contact network with a peculiar force distribution [8]. Under small deviatoric loads, an initially isotropic packing develops an anisotropic contact network because new contacts are created along the loading direction, while some are lost perpendicular to it. This geometrical anisotropy leads in turn to an anisotropic response of the granular assembly, whose effect on the anisotropic elasticity and the plasticity remains an open issue [9–11].

In this paper we combine the continuous and the discrete approaches in the investigation of the effect of the induced anisotropy on the elastoplastic response of a two-dimensional model consisting of perfect packings of polygons. The polygonal particles have exactly adjusted shapes and leave null porosity. The granular packing is regarded as two complementary networks of sliding and nonsliding contacts.

This bimodal character of the force network was suggested by *Gedankenexperimente* by Dietrich [12]. Vardoulakis [13] was next to use the idea of Dietrich by looking carefully into the force chains resulting in the numerical simulations of Cundall [14]. He produced a constitutive model that considers sand as a mixture of these two fractions [15]. This idea was later numerically verified by the observation of the buckling force chains supported by sliding lateral contacts during shear [16].

This paper is organized as follows: The details of the particle model are presented in Sec. II. The interparticle forces include elasticity and friction with the possibility of sliding. The polygonal packing is driven by applying stress controlled loading at the boundary particles. The calculation of the incremental stress-strain relation is presented in Sec. III.

*Electronic address: fernando@ica1.uni-stuttgart.de
†Electronic address: S.Luding@tnw.tudelft.nl
‡Electronic address: hans@ica1.uni-stuttgart.de
§Electronic address: vardoulakis@mechan.ntua.gr

The incremental strain is decomposed into reversible elastic and irreversible plastic parts. In Sec. IV we characterize the anisotropy of the contact network and the subnetwork of sliding contacts. In Sec. V the anisotropy induced by shearing in the contact network is correlated with the elastic tensor. In Sec. VI we discuss the plastic flow rule in the framework of several existing elastoplastic models. We also interpret the dilatancy as an effect of the induced anisotropy in the subnetwork of sliding contacts.

II. DISCRETE MODEL

Here we present a two-dimensional discrete element model which has been used to investigate different aspects of the deformation of granular materials, such as fragmentation [18], damage [19], strain localization [20,21] and cyclic loading [22]. This model consists of randomly generated convex polygons, which interact via contact forces. There are some limitations in the use of such a two-dimensional code to model granular materials that are three-dimensional in nature. These limitations have to be kept in mind in the interpretation of the results and its comparison with the experimental data. In order to give a three-dimensional picture of this model, one can consider the polygons as a collection of bricks with randomly shaped polygonal basis filling completely the space such as the case of dry masonry walls. Another physical picture of the model are the aggregates of calcite crystal granules such as in the case of marble [17]. The typical texture of marble is illustrated in Fig. 1. The deformation of individual grains, as well as the Poisson effect in the grains, are not taken into account. In the case of marble, this approximation is reasonable since deformation occurs principally in the interface between the grains [23].

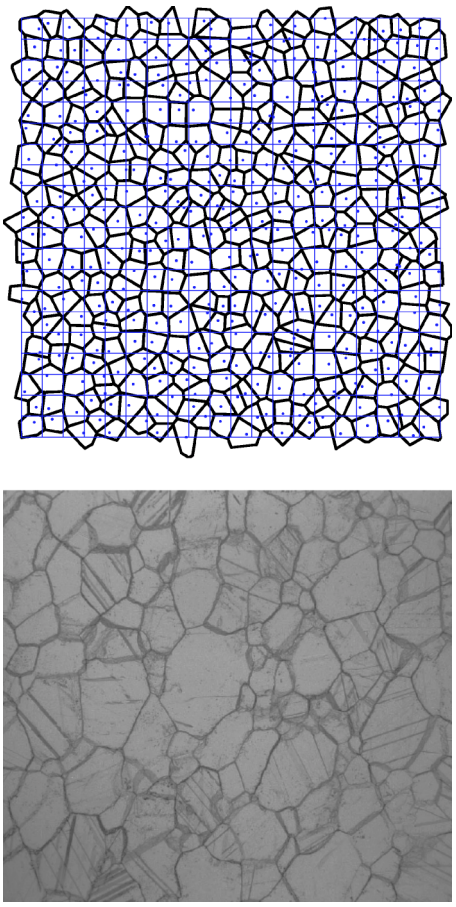

FIG. 1. Left: Voronoi construction used to generate the convex polygons. The dots indicate the point used in the tessellation. Periodic boundary conditions were used. Right: Typical texture of marble. (Courtesy of Royer-Carfagni [17].)

A. Generation of polygons

The polygons representing the particles in this model are generated by using the method of Voronoi tessellation [19]. This method is schematically shown in the left part of Fig. 1: First, a regular square lattice of side ℓ is created. Then, we choose a random point in each cell of the rectangular grid. Each polygon is constructed assigning to each point that part of the plane that is closer to it than to any other point. The details of the construction of the Voronoi cells can be found in the literature [24,25].

Using the Euler theorem, it has been shown analytically that the mean number of edges of this Voronoi construction must be 6 [25]. The number of edges of the polygons is distributed between 4 and 8 for 98.7% of the polygons. Numerically, it is shown that the orientational distribution of edges is isotropic; and the distribution of areas of polygons is symmetric around its mean value ℓ^2. The probabilistic distribution of areas follows approximately a Gaussian distribution with a variance of $0.36\ell^2$.

B. Contact forces

When two elastic bodies come into contact, a slight deformation in the contact region appears, and there is an interaction which transmits not only force but also torque between the bodies. In principle, this interaction can be obtained using standard technics such as finite elements methods. In our model this method would be computationally very expensive, and it is necessary to introduce some basic assumptions to simplify the calculation of this interaction. As it was presented before [20], realistic contact forces and torques can be obtained by allowing the polygon to overlap and calculating them from this virtual overlap.

The first step for the calculation of the contact interaction is the definition of the line representing the flattened contact line between the two polygons in contact. This is defined from the contact points resulting from the intersection of the edges of the overlapping polygons. In most cases, we have two contact points, as shown in the left of Fig. 2. In such a case, the contact line is defined by the vector $\vec{C}=\overrightarrow{C_1C_2}$ connecting these two intersection points. In some pathological cases, the intersection of the polygons leads to four or six contact points as shown in the right of Fig. 2. In these cases, we define the contact line by the vector $\vec{C}=\overrightarrow{C_1C_2}+\overrightarrow{C_3C_4}$ or $\vec{C}=\overrightarrow{C_1C_2}+\overrightarrow{C_3C_4}+\overrightarrow{C_5C_6}$, respectively. This choice guarantees a continuous change of the contact line, and therefore of the contact forces, during the evolution of the contact.

The contact force is separated as

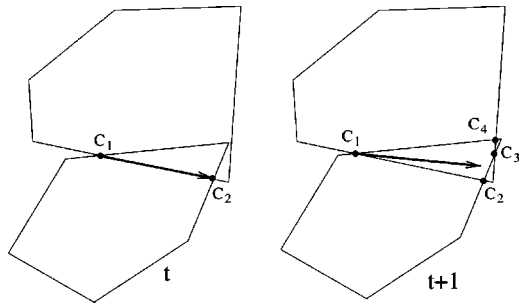

FIG. 2. Contact points C_i before (left) and after the formation of a pathological contact (right). The vector denotes the contact line. t represents the number of time steps.

$$\vec{f}^c = \vec{f}^e + \vec{f}^v, \tag{1}$$

where $\vec{f}^e$ and $\vec{f}^v$ are the elastic and viscous contribution. The elastic part of the contact force is decomposed as

$$\vec{f}^e = f_n^e \hat{n}^c + f_t^e \hat{t}^c. \tag{2}$$

The unit tangential vector is defined as $\hat{t}^c = \vec{C}/|\vec{C}|$, and the normal unit vector $\hat{n}^c$ is taken perpendicular to $\vec{C}$. The normal elastic force is calculated as

$$f_n^e = -k_n A/L_c, \tag{3}$$

where k_n is the normal stiffness, A is the overlapping area and L_c is a characteristic length of the polygon pair. Our choice is $L_c = |\vec{C}|$. This normalization is necessary to be consistent in the units of force [19].

The frictional force is calculated using an extension of the method proposed by Cundall-Strack [26]. An elastic force proportional to the elastic displacement is included at each contact

$$f_t^e = -k_t \Delta x_t^e, \tag{4}$$

where k_t is the tangential stiffness. The elastic displacement Δx_t is calculated as the time integral of the tangential velocity of the contact during the time where the elastic condition $|f_t^e| < \mu f_n^e$ is satisfied. The sliding condition is imposed, keeping this force constant when $|f_t^e| = \mu f_n^e$. The straightforward calculation of this elastic displacement is given by the time integral starting at the beginning of the contact:

$$\Delta x_t^e = \int_0^t v_t^c(t') \Theta(\mu f_n^e - |f_t^e|) dt', \tag{5}$$

where Θ is the Heaviside step function and $\vec{v}_t^c$ denotes the tangential component of the relative velocity $\vec{v}^c$ at the contact:

$$\vec{v}^c = \vec{v}_i - \vec{v}_j + \vec{\omega}_i \times \vec{\ell}_i - \vec{\omega}_j \times \vec{\ell}_j. \tag{6}$$

Here $\vec{v}_i$ is the velocity and $\vec{\omega}_i$ is the angular velocity of the particles in contact. The branch vector $\vec{\ell}_i$ connects the center of mass of particle i to the point of application of the contact force. Replacing Eqs. (3) and (4) into (2) one obtains

$$\vec{f}^e = -k_n \frac{A}{L_c} \hat{n}^c - k_t \Delta x_t^e \hat{t}^c. \tag{7}$$

Damping forces are included in order to allow rapid relaxation during the preparation of the sample, and to reduce the acoustic waves produced during the loading. These forces are calculated as

$$\vec{f}^v = -m(\gamma_n v_n^c \hat{n}^c + \gamma_t v_t^c \hat{t}^c), \tag{8}$$

being $m = (1/m_i + 1/m_j)^{-1}$ the effective mass of the polygons in contact. $\hat{n}^c$ and $\hat{t}^c$ are the normal and tangential unit vectors defined before, and γ_n and γ_t are the coefficients of viscosity. These forces introduce time dependent effects during the loading. We will show that these effects can be arbitrarily reduced by increasing the loading time, as corresponds to the quasistatic approximation.

The transmitted torque between two polygons in contact is calculated as $\vec{\tau} = \vec{\ell} \times \vec{f}$. The so-called *branch vector* is taken as the vector connecting the center of mass of the particle to the center of mass of the overlapping polygon. Since this point is not collinear with the centers of masses of the interacting polygons, there is a contribution of the torque from both components of the contact force. This makes an important difference with respect to the interaction between disks or spheres: Polygons can transmit torques even in absence of frictional forces.

C. Molecular dynamics simulation

The evolution of the position $\vec{x}_i$ and the orientation φ_i of the polygon i is governed by the equations of motion:

$$m_i \ddot{\vec{x}}_i = \sum_c \vec{f}_i^c + \sum_b \vec{f}_i^b,$$

$$I_i \ddot{\varphi}_i = \sum_c \vec{\ell}_i^c \times \vec{f}_i^c + \sum_b \vec{\ell}_i^b \times \vec{f}_i^b. \tag{9}$$

Here m_i and I_i are the mass and moment of inertia of the polygon. The first sum goes over all those particles in contact with this polygon; the second one over all the forces applied on the boundary. The interparticle contact forces $\vec{f}^c$ are given by replacing Eqs. (7) and (8) in Eq. (1). In order to perform stress controlled test, a time dependent external force is applied on each edge belonging to the external contour of the assembly: The external force $\vec{f}^b$ acting of the edge $\vec{T}^b = \Delta x_1^b \hat{x}_1 + \Delta x_3^b \hat{x}_3$, is given by

$$\vec{f}^b = -\sigma_1 \Delta x_3^b \hat{x}_1 + \sigma_3 \Delta x_1^b \hat{x}_3 - \gamma_b m_i \vec{v}^i. \tag{10}$$

Here $\hat{x}_1$ and $\hat{x}_3$ are the unit vectors of the Cartesian coordinate system. σ_1 and σ_3 are the components of the stress we want to apply on the sample. Each loading stage from the stress state σ_i^o to σ_i^f is applied as

$$\sigma_i(t) = \sigma_i^o + \frac{\sigma_i^f - \sigma_i^o}{2}\left[1 - \cos\left(\frac{2\pi t}{t_0}\right)\right], \quad i = 1,3, \tag{11}$$

where t_0 is the time of loading. This modulation is chosen to avoid acoustic waves at the starting and at the end of the

loading. The loading is applied in a quasistatic way in the sense that a faster (or slower) loading has no detectable effect. Note that a much faster loading has strong influence and a much slower loading would take much longer. Therefore our "quasi"-static loading is a compromise between computational and physical demands.

We use a fifth-order Gear predictor-corrector method for solving the equation of motion [27]. This algorithm consists of three steps. The first step predicts position and velocity of the particles by means of a Taylor expansion. The second step calculates the forces as a function of the predicted positions and velocities. The third step corrects the positions and velocities in order to optimize the stability of the algorithm. This method is much more efficient than the simple Euler approach or the Runge-Kutta method, especially for problems where very high accuracy is a requirement.

There are many parameters in the molecular dynamics algorithm. Before choosing them, it is convenient to make a dimensional analysis. In this way, we can keep the scale invariance of the model and reduce the parameters to a minimum of dimensionless constants. There is one dimensionless parameter, the friction coefficient, and there are 10 dimensional parameters. The latter ones can be reduced by introducing the following characteristic times: the loading time t_0, the relaxation times $t_n=1/\gamma_n$, $t_t=1/\gamma_t$, $t_b=1/\gamma_b$ and the characteristic period of oscillation $t_s=\sqrt{\rho\ell^2/k_n}$ of the normal contact.

Using the Buckingham Pi theorem [28], one can show that the strain response, or any other dimensionless variable measuring the response of the assembly during loading, depends only on the following dimensionless parameters: $\alpha_1=t_n/t_s$, $\alpha_2=t_t/t_s$, $\alpha_3=t_b/t_s$, $\alpha_4=t_0/t_s$, the ratio k_t/k_n between the stiffnesses, the friction coefficient μ and the ratio p_0/k_n between the confining pressure and the normal stiffness.

The variables α_i act as *control parameters*. They are chosen in order to satisfy the following criteria: (1) guarantee the stability of the numerical solution, (2) optimize the time of the calculation, and (3) satisfy the quasistatic approximation. $\alpha_1=0.1$, $\alpha_2=0.5$ and $\alpha_3=0.5$ were taken large enough to have a high dissipation, but not too large to keep the numerical stability of the method. The ratio $\alpha_4=t_0/t_s=10000$ was chosen large enough to avoid rate-dependence in the mechanical response, corresponding to the quasistatic approximation. Technically, this is performed by looking for the value of α_4 such that a reduction of it by a factor two makes a change of the stress-strain relation of less than 5%. The time step is taken as $\Delta t=0.1t_s$.

The parameters k_n, k_t/k_n and μ can be considered as *material parameters*. They determine the constitutive response of the system, so they should be adjusted to the experimental data. The initial slope of the stress-strain curve of the material is linearly related to the value of normal stiffness of the contact. The ratio p_0/k_n determines the characteristic overlapping length δ between the polygons as follows: From the balance between external forces and contact forces in a pressure confined granular assembly one obtain that $p_0\ell\sim k_n\delta$, so that the ratio between the elastic deflection and the mean diameters of the polygons satisfies $\delta/\ell\sim p_0/k_n$. In order to guaranty overlapping lengths lower that 1% of the diameter of the polygons we choose $p_0/k_n\leqslant 0.004$. The plastic deformations before failure as well as the Poisson ratio of the assembly are monotonic decreasing function of the ratio k_t/k_n. For samples subjected to isotropic pressure, taking values of k_t between 0 and k_n lead to Poisson ratios between 0.35 and 0.0. Our choice $k_t=0.33k_n$ gives a Poisson ratio of $\nu_0=0.07$. This is calculated from the elastic response in Sec. V. Smaller values of k_t lead to larger Poisson ratios, but also to larger plastic deformations which in turn induce time dependence effects and hence very expensive quasistatic simulations.

The angles of friction and dilatancy are increasing functions of the interparticle friction coefficient μ. Taking values of μ between 0 and 5.0 yields friction angles between 6° and 60° [29]. This range should be compared to the friction angle of 48.2° measured in experiments with marble [30], that is bigger than the value of 40°–45° measured in sand [31]. The reason of this difference is that the interlocking between the grains in marble is bigger than in sand. A friction coefficient of $\mu=0.25$ is chosen in the simulations. This lead to dilatancy angles between 20° and 30° [21]. Triaxial tests on marble lead dilatancy angles between 11° and 38° [30], whereas in sand they yield angles between 7° and 14° [31]. Note that the dilatancy angles in marble are bigger than in sand. This is due to the peculiar texture of marble with vanishing void ratio, which is well captured by our model.

III. INCREMENTAL RELATION

When a granular material is loaded, the dynamics of the contact network involves creation and loss of contacts as well as restructuring by means of sliding contacts [32]. These changes imply a continuous variation of the stress-strain relation and a change of the void ratio during load [33,34]. This behavior becomes apparent if a polygonal packing confined by isotropic pressure is submitted to vertical load with constant velocity [35]. The dependence of the deviatoric stress $\sigma_1-\sigma_3$ and the volumetric strain $e=\Delta V/V$ on the axial strain $\epsilon_1=\Delta H/H$ are shown in Fig. 3 for different confining pressures. We observe a compaction regime where there are almost no open contacts and the restructuring is given only by sliding contacts. The stress response is characterized by a continuous decrease of the slope of the stress-strain curve from the very beginning of the load process. Even in this extreme case of dense polygonal packings, any load rearranges the contact network by means of sliding contacts, which in turn reduces the strength of the material. Before failure the sample undergoes a transition from compactancy to dilatancy. This transition is caused by loss of contacts perpendicular to the load direction, allowing the contact network to rearrange and inducing large plastic deformations. Near to the failure, the amount of plastic deformations is much larger than the elastic ones. This reduces considerably the value of the stiffness with respect to its initial value. After failure the sample reaches a stage where the deviatoric stress as well as the density keeps approximately constant except for some fluctuations remaining for large deformations. The continuous variation of the stress-strain curve with the loading makes it necessary to use an incremental formalism in the description of the mechanical response.

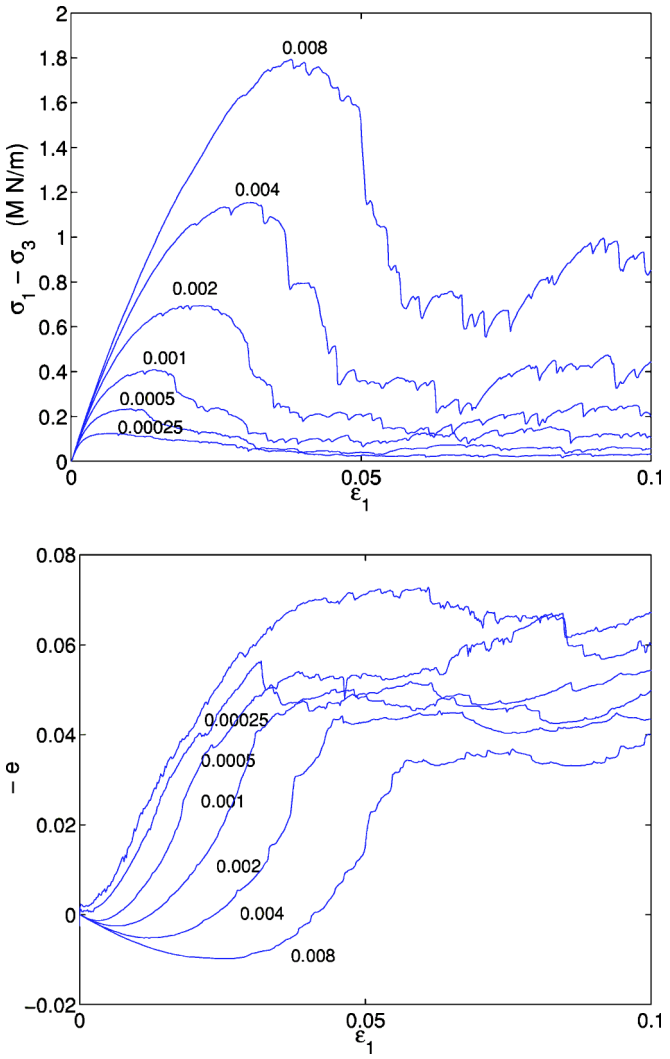

FIG. 3. Deviatoric stress and volumetric strain versus axial strain for different values of p/k_n, where p is the lateral pressure. $e>0$ represents compression of the sample.

A. Theoretical framework

We introduce here some definitions required for the determination of the incremental response of the polygonal packing. The calculation of the average of the Cauchy stress tensor over a granular assembly leads to [36]

$$\sigma_{ij} = \frac{1}{A}\sum_b r_i^b f_j^b. \tag{12}$$

The sum goes over all the forces acting over the boundary of the assembly. A is the area enclosed by the boundary and $\vec{r}^b$ is the point of application of the boundary force $\vec{f}^b$ given by Eq. (10). The boundary of the assembly is given by an irregular polygon whose vertices are denoted by $B_i=(x_i^b,y_i^b)$, where $i=1, 3$, $b=1,\ldots, N_b$, and N_b is the number of boundary segments. Using the equilibrium condition $\vec{v}_i=0$ in Eq. (10), we obtain

$$f_i^b = -\sigma_1 \Delta x_3^b \hat{x}_1 + \sigma_3 \Delta x_1^b \hat{x}_3, \tag{13}$$

where $\Delta x_i^b = x_i^{b+1} - x_i^b$. The point of application of this force is given by the center of the edge:

$$\vec{r}^b = \frac{1}{2}(x_1^{b+1} + x_1^b)\hat{x}_1 + \frac{1}{2}(x_3^{b+1} + x_3^b)\hat{x}_3. \tag{14}$$

Replacing Eqs. (13) and (14) into Eq. (12) leads to

$$\sigma = \frac{1}{2A}\begin{bmatrix} -\sigma_1 \sum_b (x_1^{b+1} + x_1^b)\Delta x_3^b & \sigma_3 \sum_b (x_1^{b+1} + x_1^b)\Delta x_1^b \\ -\sigma_1 \sum_b (x_3^{b+1} + x_3^b)\Delta x_3^b & \sigma_3 \sum_b (x_3^{b+1} + x_3^b)\Delta x_1^b \end{bmatrix}. \tag{15}$$

By expanding this sums and using the formula for the area of irregular polygons

$$A = \frac{1}{2}\sum_b (x_1^b x_3^{b+1} - x_1^{b+1} x_3^b), \tag{16}$$

one obtains

$$\sigma = \begin{bmatrix} \sigma_1 & 0 \\ 0 & \sigma_3 \end{bmatrix}. \tag{17}$$

Thus the stress controlled test is restricted to stress states without off-diagonal components. We can simplify the notation introducing the *pressure* p and the *deviatoric stress* q in the components of the *stress vector*

$$\tilde{\sigma} = \begin{bmatrix} p \\ q \end{bmatrix} = \frac{1}{2}\begin{bmatrix} \sigma_1 + \sigma_3 \\ \sigma_1 - \sigma_3 \end{bmatrix}. \tag{18}$$

The stress should be accompanied with a micromechanical expression for the strain tensor. This is given by the average of the gradient of the displacement field over the assembly [37]. Different from round grains, the length of the contact region at the polygons is not necessarily much smaller than their diameter. There is therefore a displacement field which should be different from the case of a packing of spheres. However, It is shown in [38] that the incremental strain tensor can be transformed into a line integral of the displacement field on the external boundary of the polygonal packing, so that it does not depend on the displacement field inside of the packing. By assuming rigid body motion at the boundary particles, the line integral leads to a sum over the boundary segments of the sample [38]

$$d\epsilon_{ij} = \frac{1}{2A}\sum_b (du_i^b N_j^b + du_j^b N_i^b). \tag{19}$$

Here $d\vec{u}^b$ is the displacement of the boundary segment, that is calculated from the linear displacement $d\vec{x}$ and the angular rotation $d\vec{\phi}$ of the polygons belonging to it, according to

$$d\vec{u}^b = d\vec{x} + d\vec{\phi} \times \vec{\ell}. \tag{20}$$

From the eigenvalues $d\epsilon_1$ and $d\epsilon_3$ of $d\epsilon_{ij}$ we define the *volumetric* and *deviatoric* components of the strain as the components of the *incremental strain vector*:

TABLE I. Principal modes of loading according to the orientation of $\hat{\theta}$.

θ	TEST	
0°	isotropic compression	$dp>0$ $dq=0$
45°	axial loading	$d\sigma_1>0$ $d\sigma_3=0$
90°	pure shear	$dp=0$ $dq>0$
135°	lateral loading	$d\sigma_1=0$ $d\sigma_3>0$
180°	isotropic expansion	$dp<0$ $dq=0$
225°	axial stretching	$d\sigma_1<0$ $d\sigma_3=0$
270°	pure shear	$dp=0$ $dq<0$
315°	lateral stretching	$d\sigma_1=0$ $d\sigma_3<0$

$$d\tilde{\epsilon} = \begin{bmatrix} de \\ d\gamma \end{bmatrix} = - \begin{bmatrix} d\epsilon_1 + d\epsilon_3 \\ d\epsilon_1 - d\epsilon_3 \end{bmatrix}. \tag{21}$$

By convention $de>0$ corresponds to a compression of the sample. We assume a rate-independent relation between the incremental stress and incremental strain tensor. In this case the incremental relation can generally be written as [39]

$$d\tilde{\epsilon} = M(\hat{\theta}, \tilde{\sigma}) d\tilde{\sigma}, \tag{22}$$

where $\hat{\theta}$ is the unit vector defining a specific direction in the stress space:

$$\hat{\theta} = \frac{d\tilde{\sigma}}{|d\tilde{\sigma}|} \equiv \begin{bmatrix} \cos\theta \\ \sin\theta \end{bmatrix}, \quad |d\tilde{\sigma}| = \sqrt{dp^2 + dq^2}. \tag{23}$$

The constitutive relation results from the calculation of $d\tilde{\epsilon}(\theta)$, where each value of θ is related to a particular mode of loading. Some special modes are listed in Table I.

The comparison of the incremental response with the constitutive models requires to select the theoretical framework which fits best to the numerical data. Many constitutive models can be found in the market, but they are essentially divided into two groups [39]: The ***incremental nonlinear*** models assume that the dependence of M on θ is nonlinear, prototype of this class being the hypoplastic models [40]. The second group corresponds to the ***incremental piecewise linear*** models, such as the ***elastoplastic*** models. In these models the space of the stress directions can be divided into regions where the incremental relation is strictly linear [41].

A special feature of the incremental nonlinear models is that they depart from the superposition principle, i.e., if one decomposes an incremental load as $d\tilde{\sigma}=d\tilde{\sigma}_\alpha+d\tilde{\sigma}_\beta$, the strain response of the total load is different from the sum of the strain responses of the two incremental loads [39,40]. Numerical simulations with polygonal packings show that the superposition principle is accurately satisfied [42], suggesting that the incremental piecewise linear models are more appropriate to interpret our simulations. This conclusion is also supported by the fact that the strain envelope response consists of two pieces of ellipses, as we will see later.

In order to compare the incremental response to the elastoplastic models, it is necessary to assume that the incremental strain can be separated into an elastic (recoverable) and a plastic (unrecoverable) component:

$$d\tilde{\epsilon} = d\tilde{\epsilon}^e + d\tilde{\epsilon}^p, \tag{24}$$

$$d\tilde{\epsilon}^e = D^{-1}(\tilde{\sigma}) d\tilde{\sigma}, \tag{25}$$

$$d\tilde{\epsilon}^p = J(\theta, \tilde{\sigma}) d\tilde{\sigma}. \tag{26}$$

Here, D^{-1} is the inverse of the stiffness tensor D, and $J=M-D^{-1}$ the flow rule of plasticity [43]. They will be obtained from the calculation of $d\tilde{\epsilon}^e(\theta)$ and $d\tilde{\epsilon}^p(\theta)$.

B. Calculation of the incremental response

The method presented here to calculate the strain response has been used on sand experiments [44]. It was introduced by Bardet [45] in the calculation of the incremental response using discrete element methods. This method will be used to determine the elastic $d\tilde{\epsilon}^e$ and plastic $d\tilde{\epsilon}^p$ components of the strain as function of the stress state $\tilde{\sigma}$ and the stress direction $\hat{\theta}$. First, the sample is isotropically compressed until it reaches the stress value $\sigma_1=\sigma_3=p-q$. Then, it is subjected to axial loading in order to increase the axial stress σ_1 to $p+q$. Loading the sample from $\tilde{\sigma}$ to $\tilde{\sigma}+d\tilde{\sigma}$ the strain increment $d\tilde{\epsilon}$ is obtained. Then the sample is unloaded to $\tilde{\sigma}$ and one finds a remaining strain $d\tilde{\epsilon}^p$, that corresponds to the plastic component of the incremental strain. For small stress increments the unload stress-strain path is almost elastic. Thus the difference $d\tilde{\epsilon}^e=d\tilde{\epsilon}-d\tilde{\epsilon}^p$ can be taken as the elastic component of the strain. This procedure is implemented on different *clones* of the same sample, choosing different stress directions and the same stress amplitude in each one of them.

The method is based on the assumption that the strain response after a reversal loading is completely elastic. Numerical simulations have shown that this assumption is not strictly true, because sliding contacts are always observed during the unload path [22,46]. In our simulations, we observe that for stress amplitudes of $|d\tilde{\sigma}|=0.001p$ the plastic deformation during the reversal stress path is less than 1% of the corresponding value of the elastic response. Within this margin of error, the method proposed by Bardet can be taken as a reasonable approximation to describe the elastoplastic response.

Figure 4 shows the load-unload stress paths and the corresponding strain response when an initial stress state with $\sigma_1=1.25\times10^{-3}k_n$ and $\sigma_3=0.75\times10^{-3}k_n$ is chosen. The end of the load paths in the stress space maps into a strain envelope response $d\tilde{\epsilon}(\theta)$ in the strain space. Likewise, the end of the unload paths maps into a plastic envelope response $d\tilde{\epsilon}^p(\theta)$. This envelope consists of a very thin ellipse, nearly a straight line, which confirms the unidirectional aspect of the irreversible response predicted by the elastoplasticity theory [43]. The *yield direction* ϕ can be found from this response, as the direction in the stress space where the plastic response is maximal. In this example, this is around $\phi=87.2°$. The *flow direction* ψ is given by the direction of the maximal plastic response in the strain space, which is around 76.7°.

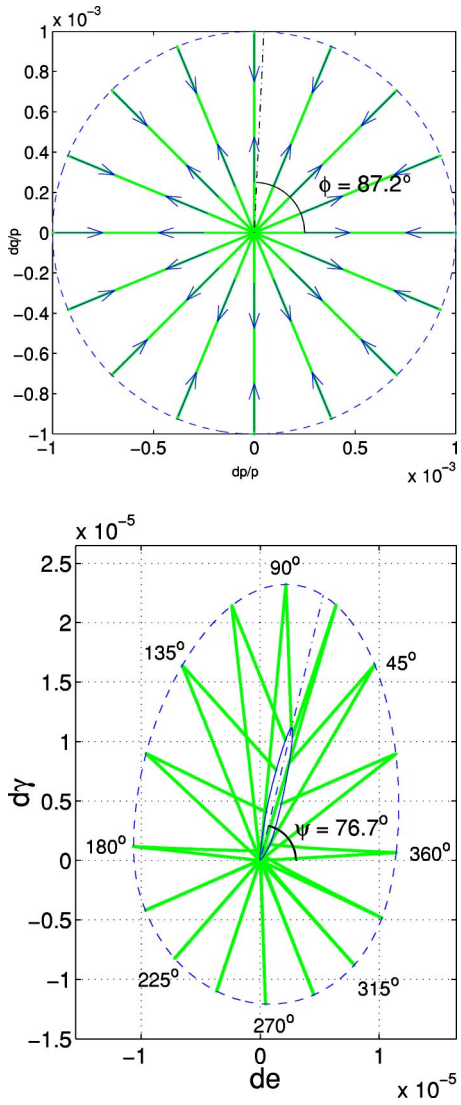

FIG. 4. Stress-strain relation resulting from the load-unload test. Grey solid lines are the paths in the stress and strain spaces. Grey dash-dotted lines represent the yield direction (upper) and the flow direction (lower). Dashed line shows the strain envelope response and the solid line is the plastic envelope response.

The fact that these directions do not agree reflects a *nonassociated flow rule*, that is also observed in experiments on realistic soils [44].

Another interesting aspect of the incremental stress-strain relation concerns the elastic response $d\tilde{\epsilon}^e = d\tilde{\epsilon} - d\tilde{\epsilon}^p$. Figure 5 shows the elastic envelope response for different stress ratios. For stress values such as $q/p \leqslant 0.4$ the stress envelope responses collapse on to the same ellipse. This response can be described by the isotropic linear elasticity by introducing two material parameters i.e. the Young modulus E and the Poisson ratio ν [47]. For stress values satisfying $q/p > 0.4$ there is a reduction of the stiffness, and a rotation of the principal directions of the elastic tensor. In this case, the elastic response can not be described using these two parameters.

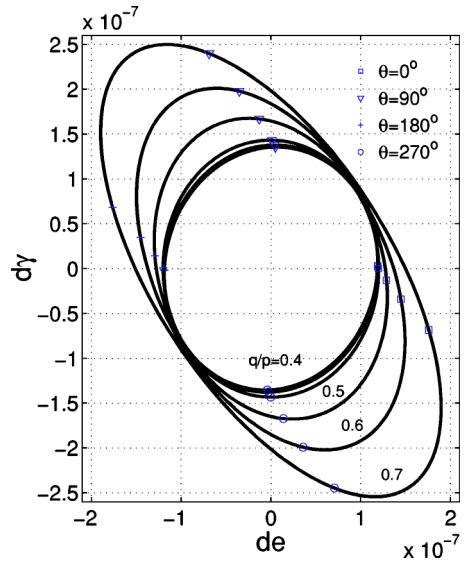

FIG. 5. Elastic strain envelope responses $d\tilde{\epsilon}^e(\theta)$. They are calculated for a pressure $p=0.001k_n$ and taking deviatoric stresses with $q=0.0p$ (inner), $0.1p,\ldots,0.7p$ (outer).

IV. ANISOTROPY

It is not surprising that isotropic linear elasticity is not valid in the deformation of samples subjected to deviatoric loads. Indeed, numerical simulations [33,34,48–50] and photo-elastic experiments [51,52] on granular materials show that loading induces a significant deviation from isotropy in the contact network. The structural changes of contact network involve creation of contacts whose branch vectors are oriented nearly parallel to the loading direction, opening of contacts perpendicular to the loading direction, and redistribution of contacts by rolling and slippage. The first two processes reduce the strength under lateral compression below the strength under further horizontal load, so that the elastic response becomes anisotropic [33,34,48,50]. The rearrangements by sliding contacts play an important role in the plasticity, which has not been much explored by date. In this section we present a statistical investigation of the anisotropy of the contact network and the subnetwork of sliding contacts. The calculations were performed taking 10 different assemblies of 20×20 polygons.

A. Anisotropy of the contact network

The anisotropy of the granular sample can be characterized by the distribution of the orientations of the branch vectors $\vec{\ell}$. Each branch vector connects the center of mass of the polygon to the center of application of the contact force. Parts (a) and (b) of Fig. 6 shows the branch vectors of the polygonal packing for two different stages of loading. The structural changes of micro-contacts are principally due to the opening of contacts whose branch vectors are oriented nearly perpendicular to the loading direction. The onset of anisotropy can be investigated by defining $\Omega(\varphi)\Delta\varphi$ as the number of contacts per particle whose branch vector is oriented between the angles φ and $\varphi+\Delta\varphi$, measured with re-

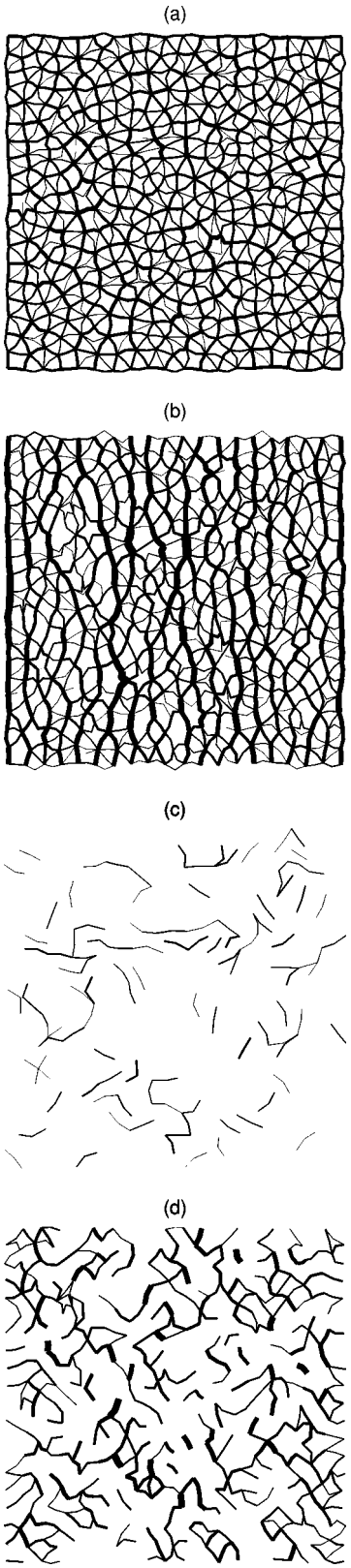

FIG. 6. The lines show the branch vectors of the contact network for $\sigma_1=\sigma_3=0.001k_n$ (a) and $\sigma_1=0.65\times10^{-3}k_n$ and $\sigma_3=0.35\times10^{-3}k_n$ (b). The branch vectors of the subnetwork of sliding contacts are shown for the isotropic (c) and the anisotropic (d) case. The width of the lines represents the normal force.

spect to the direction along which the sample is loaded. The right part of Fig. 7 shows this distribution for three different stages of loading. Note that anisotropy is absent for small deviatoric loads, and it appears only near to failure. For all stress values, the orientational distribution can be accurately described by a truncated Fourier series expansion:

$$\Omega(\varphi) \approx \frac{N_0}{2\pi}[a_0 + a_1\cos(2\varphi) + a_2\cos(4\varphi)]. \qquad (27)$$

Here $N=N_0a_0$ is the average coordination number of the polygons, whose initial value $N_0=6.0$ reduces as the load is increased. The parameters a_1 and a_2 are related to the second and fourth order fabric tensors defined in other works to characterize the orientational distribution of the contacts [32,48,53]. We will call them *fabric coefficients*. The dependence of the fabric coefficients on the stress ratio q/p is shown in Fig. 8. We observe that for stress states satisfying $q<0.4p$ there are almost no open contacts. Above this limit a significant number of contacts are open, leading to an anisotropy in the contact network. Fourth order terms in the Fourier expansion are necessary in order to accurately describe this distribution.

Of course, the onset of anisotropy depends on the initial distribution of contact forces, and its evolution during loading. Figure 7 shows the distribution of contact forces in the polygonal assemblies for three different stages of loading an the corresponding orientational distributions. For low stress ratios, the contact forces is rather concentrated around their mean value. This distribution is qualitatively different from the heterogeneous distribution of forces observed in polydisperse disks packings [8,54]. This is due to the particular geometry of the polygonal packing, where the absence of voids and the low polydispersity of the grains reduces the disorder of the contact network.

From Fig. 7 we observe that loading induces an increase of the fluctuations of contact forces and hence opening of contacts when the normal force f_n vanishes. In particular, for stress values satisfying $q<0.4p$ there is almost no open contacts. Above this limit a significant number of contacts are open, leading to an anisotropy in the contact network. This is different from the findings obtained for disks packings, where due to the round nature of the particles that do not resist against deformations as the polygons do, the anisotropy starts to grow already for small deviatoric deformations [33,34].

B. Anisotropy of the sliding contacts

Let us classify the branch vectors of the contact network in two classes, the first class corresponds to the nonsliding contacts, which are able to carry the load in the material. The second class is given by the sliding contacts, which allow the rearrange of the contact network during loading.

The sliding condition at the contacts is given by $|f_t|=\mu f_n$, where f_n and f_t are the normal and tangential components of the contact force, and μ is the friction coefficient. When the sample is isotropically compressed, we observe a significant number of contacts reaching the sliding conditions. If the sample has not been previously sheared, the

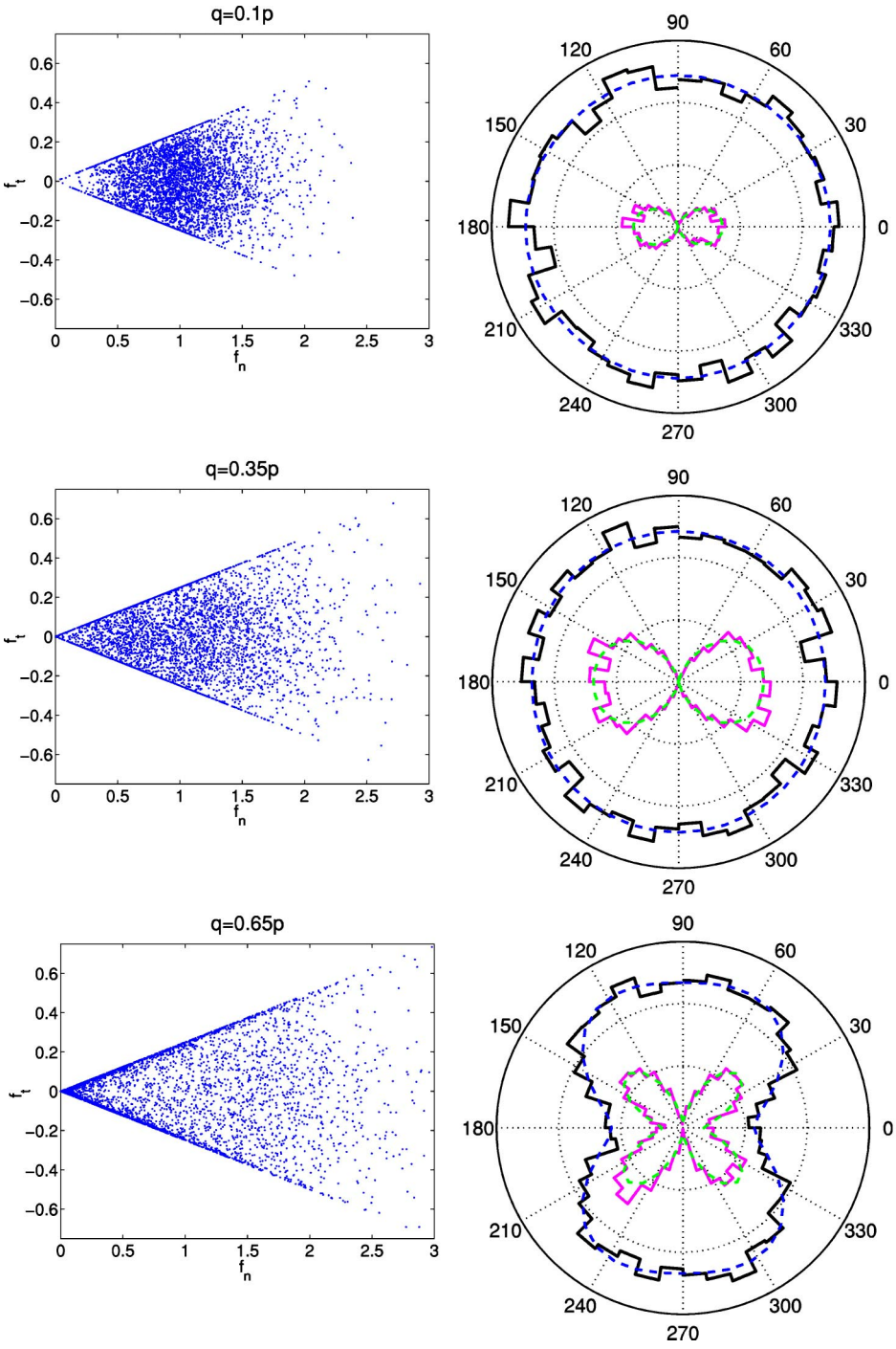

FIG. 7. Left: force distribution for the stress ratios $q/p=0.1$, 0.35, and 0.65. Here f_t and f_n are the tangential and normal components of the force. They are normalized by the mean value of f_n. Right: orientational distribution of the contacts $\Omega(\varphi)$ (outer) and of the sliding contacts $\Omega^s(\varphi)$ (inner). φ represents the orientation of the branch vector.

subnetwork of sliding contacts is isotropic as shown the part (c) of Fig. 6. This isotropy is broken when the sample is subjected to deviatoric loads, as shown part (d) of Fig. 6. The onset of anisotropy is investigated by introducing the polar function $\Omega^s(\varphi)$, where $\Omega^s(\varphi)\Delta\varphi$ is the number of sliding contacts per particle whose branch vector is oriented between φ and $\varphi+\Delta\varphi$.

Figure 7 shows the orientational distribution of sliding contacts for different stress ratios. For low stress ratios, the branch vectors $\vec{\ell}$ of the sliding contacts are oriented nearly perpendicular to the loading direction. Increasing the deviatoric strain results in an increase of the number of the sliding contacts and the average of the orientations of the branch vectors with respect to the load direction decreases with the stress ratio. Close to the failure, some of the sliding contacts whose branch vectors are nearly parallel to the loading direction open, giving rise to a butterfly shape distribution, as shown in Fig. 7.

The orientational distribution of the subnetwork of sliding contacts can be approximated by a truncated Fourier expansion:

$$\Omega^s(\varphi) \approx \frac{N_0}{2\pi}[c_0 + c_1\cos(2\varphi) + c_2\cos(4\varphi)]. \qquad (28)$$

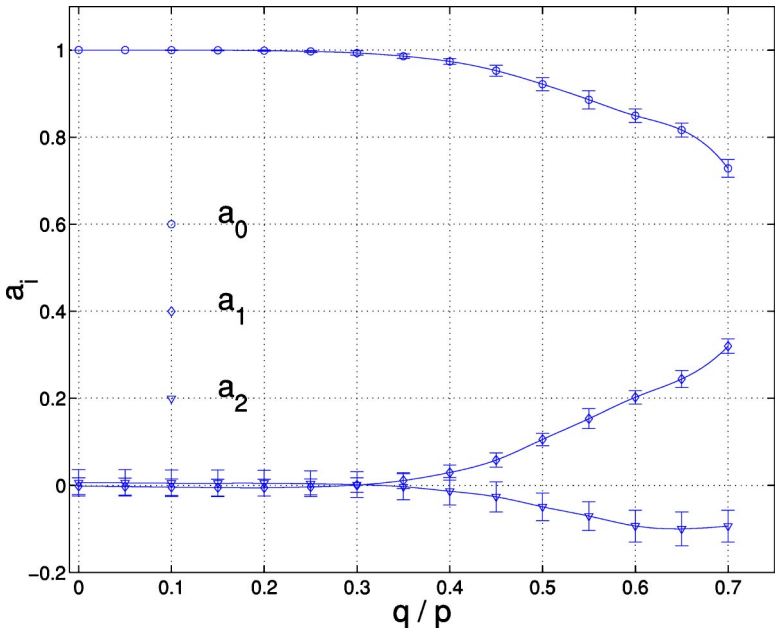

FIG. 8. Fabric coefficients of the contact network. They are defined in Eq. (27). The lines show the spline interpolation of the data.

Figure 9 shows the dependence of these fabric coefficients, measuring the induced anisotropy of the sub-network of sliding contacts. By integrating Eq. (28) over all orientation one can see that c_0 is related to the fraction of sliding contact as $n_s = c_0/a_0$. where a_0 is defined by Eq. (27). The last two coefficients measure the second and the fourth order degrees of anisotropy of the subnetwork of sliding contact. The complex dependence of this coefficients on the stress is given by the fact the number of sliding contact increases for small stress ratio, and an important fraction of them are open before failure, as it was shown in Fig. 7. Note also that for extremely small deviatoric loads the fabric coefficient c_2 is different from zero. This reflects a surprising fact: At the very beginning of the loading, most of the sliding contacts whose branch vector is oriented nearly parallel to the direction of the loading, leave the sliding condition. We will see that this abrupt induced anisotropy has an interesting effect on the plastic deformations.

V. ANISOTROPIC ELASTICITY

In this section we investigate the effect of the anisotropy of the contact network on the elastic response of the material. The most general linear relation between the incremental stress and the incremental elastic strain for anisotropic materials is given by

$$d\sigma_{ij} = D_{ijkl} d\epsilon^e_{kl}, \tag{29}$$

where D_{ijkl} is the stiffness tensor [33,34,47]. Since the stress and the strain are symmetric tensors, one can reduce their number of components from 4 to 3, and the number of com-

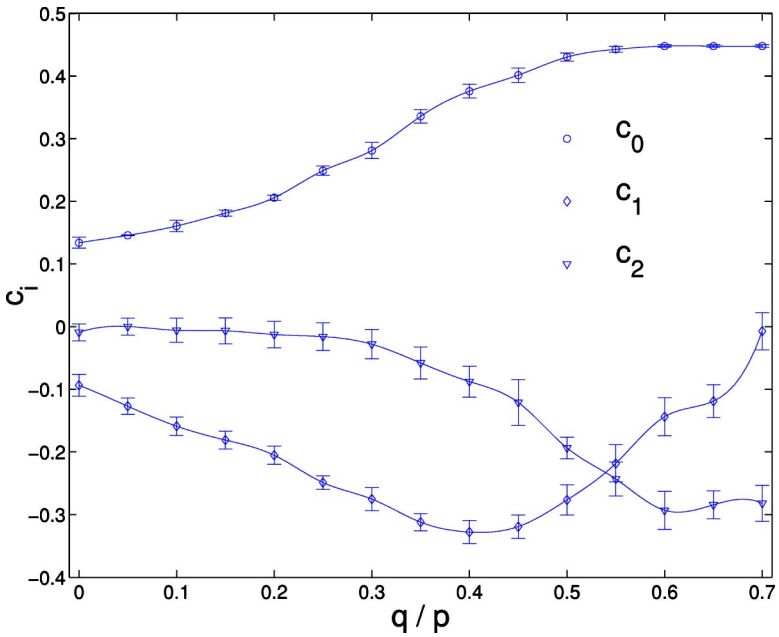

FIG. 9. Fabric coefficients of the distribution of the branch vectors of the sliding contacts. They are defined in Eq. (28). The lines show the spline interpolation of the data.

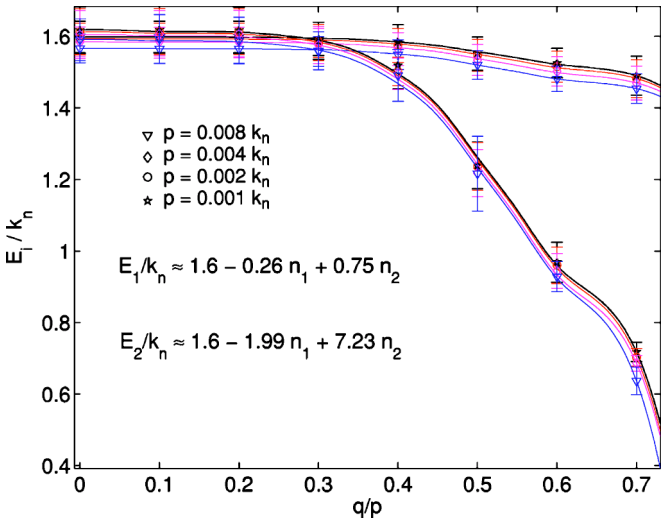

FIG. 10. Young moduli. The lines are the linear fits of $E(n_i)$ according to Eq. (33).

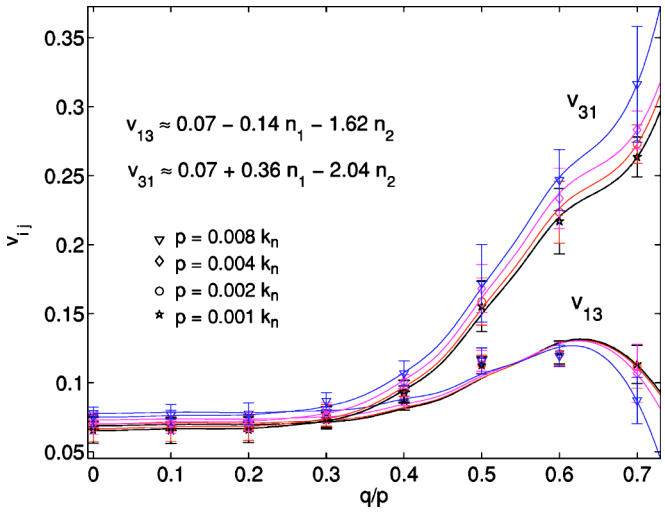

FIG. 11. Poisson ratios. The lines are the linear approximation of $\nu(n_i)$. See Eq. (33).

ponents of the stiffness tensor from 16 to 9. Elasticity involves an elastic potential energy, whose existence implies the so-called Voigt symmetry of the elastic tensor $D_{ijkl}=D_{klij}$ [55]. This symmetry reduces the constants from 9 to 6. In the particular case of isotropic materials, it has been shown that the number of constants can be reduced to 2 [47]:

$$d\epsilon_{ij}^{e}=\frac{1}{E}[(1-\nu)d\sigma_{ij}-\nu\delta_{ij}d\sigma_{kk}]. \tag{30}$$

Here E is the Young modulus and ν the Poisson ratio. δ_{ij} is the Kronecker delta. In the general case of anisotropic materials, the 6 constants are given by two Young moduli, two Poisson ratios and two shear moduli. If we consider deformations whose stress tensor has no off-diagonal components, only the Young moduli and the Poisson ratios are needed:

$$\begin{bmatrix} d\epsilon_1^e \\ d\epsilon_3^e \end{bmatrix} = \begin{bmatrix} \frac{1}{E_1} & -\frac{\nu_{13}}{E_2} \\ -\frac{\nu_{31}}{E_1} & \frac{1}{E_2} \end{bmatrix} \begin{bmatrix} d\sigma_1 \\ d\sigma_3 \end{bmatrix}. \tag{31}$$

From the elastic part of the strain envelope response one can determine these constants as shown in the Appendix. Figures 10 and 11 show these variables for different stress values. The averaged values on five different samples of 20×20 polygons are used in these calculations; the bars representing the standard variation of the data. For the stress values where the contact network is isotropic both Young moduli and Poisson ratio are the same, as corresponds to the isotropic linear elasticity. For stress ratio where the contact network depart from isotropy both Young moduli and Poisson ratios are different. Note that the reduction of the Young modulus E_i reflect the reduction of the stiffness under lateral compression, which is due to the opening of contacts whose branch vectors are almost perpendicular to the loading direction.

The correlation between the parameters of the stiffness tensor and the fabric coefficients of Eq. (27) is evaluated by introducing three parameters measuring the degree of anisotropy

$$n_0 \equiv 1-a_0, \quad n_1 \equiv a_1, \quad n_2 \equiv a_2, \tag{32}$$

where a_i are the fabric coefficients defined by Eq. (27). By integrating this equation over all orientations one obtains that $n_0=(N_0-N)/N_0$, which represents the percentage change of the average coordination number. The last two terms in Eq. (32) measure the second and the fourth order degrees of anisotropy. From Fig. 8 one obtains that $1-a_0\approx1.6a_1$. Thus, one can take n_1 and n_2 as the two independent internal variables measuring the anisotropy of the contact network. The dependence of the parameters of the stiffness tensor on these variables is evaluated by developing the Taylor series around the isotropic case where $n_i=0$

$$E_i = E_0 + E_i^1 n_1 + E_i^2 n_2 + O(n_i n_j),$$

$$v_{ij} = v_0 + v_{ij}^1 n_1 + v_{ij}^2 n_2 + O(n_i n_j). \tag{33}$$

The variables n_i are calculated as functions of q/p by performing spline interpolation of the fabric coefficients a_i in Fig. 8. Then, the coefficients in Eq. (33) are calculated from the best fit of those expansions. Figures 10 and 11 show that the linear approximation is good enough to reproduce the dependence of the stiffness on the stress ratio. This correlation is consistent with several models relating stiffness with the fabric of the contact network [32,48,53,56,57]. We observe a slight dependence of the stiffness on the pressure level which tends to vanish in the limit of small values of p/k_n. Since we use a linear relation for the contact force one would expect no dependence on the pressure. This is a spurious effect resulting from the interpenetration between the polygons. Due to the overlapping, the area occupied by all polygons under isotropic pressure is lower than the sum of their areas. This is reflected by a dependence of the stress on the pressure in a factor which is proportional to p/k_n. In

order to avoid this effect it is necessary to take small values of p/k_n. Note that for real granular materials elastic moduli—as deduced from the velocity of sound—increase with confining pressure due to the nonlinear contact elasticity. Future modeling of elastic properties should in fact involve more realistic contact force laws.

VI. PLASTIC DEFORMATION

We now turn to the description of the plastic part of the strain response. Figure 4 shows that the plastic envelope response lies almost on a straight line, as is predicted by the hardening elastoplasticity theory [1]. This motivates us to obtain the flow rule of Eq. (26) by introducing the same parameters describing the plasticity in this theory: The yield direction ϕ, the flow direction ψ, and the plastic modulus h. The yield direction is defined from the plastic envelope response as the direction in the stress space leading to maximal plastic deformation

$$|d\tilde{\epsilon}^p(\phi)| = \max_{\theta} |d\tilde{\epsilon}^p(\theta)|. \tag{34}$$

The flow direction is the orientation of the plastic response at its maximum value

$$\psi = \angle[d\tilde{\epsilon}^p(\phi)]. \tag{35}$$

The plastic modulus is obtained from the maximal plastic response

$$\frac{1}{h} = \frac{|d\tilde{\epsilon}^p(\phi)|}{|d\tilde{\sigma}|}. \tag{36}$$

The incremental plastic response can be expressed in terms of these quantities as follows: Let us define the unitary vectors $\hat{\psi}$ and $\hat{\psi}^{\perp}$. The first one is oriented in the direction of ψ and the second one is the rotation of $\hat{\psi}$ of 90°. The plastic strain is written as

$$d\tilde{\epsilon}(\theta) = \frac{1}{h}[\kappa_1(\theta)\hat{\psi} + \kappa_2(\theta)\hat{\psi}^{\perp}], \tag{37}$$

where $\kappa_1(\theta)$ and $\kappa_2(\theta)$ are defined by the dot products:

$$\kappa_1(\theta) = h(d\tilde{\epsilon}^p \cdot \hat{\psi}),$$

$$\kappa_2(\theta) = h(d\tilde{\epsilon}^p \cdot \hat{\psi}^{\perp}). \tag{38}$$

These functions are calculated from the resulting plastic response taking pressures with $p/k_n = 0.001$, 0.002, 0.004, 0.008 and deviatoric stresses with $q/p = 0.1, \ldots, 0.7$. The results are shown in Fig. 12. We found that the functions $\kappa_1(\theta - \phi)$ collapse on to the same curve for all the stress states. This curve fits well to a cosine function, truncated to zero for the negative values. The profile κ_2 depends on the stress ratio we take. This dependency is difficult to evaluate, because the values of this function are of the same order as the statistical fluctuations. In order to simplify the description of the plastic response, the following approximation is made:

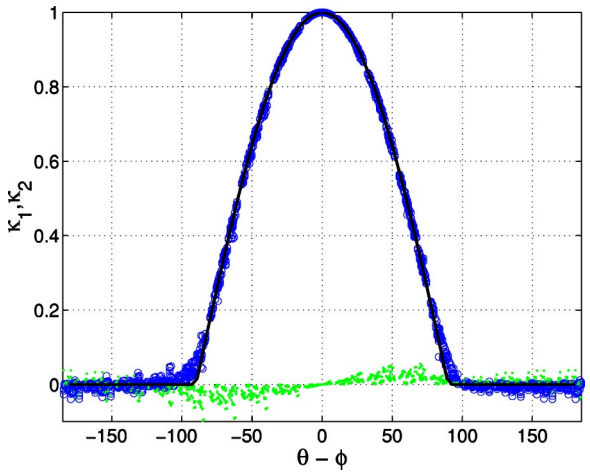

FIG. 12. Plastic components $\kappa_1(\theta)$ (circles) and $\kappa_2(\theta)$ (dots) given by Eq. (38). The results for different stress values have been superposed. The solid line represents the truncated cosine function.

$$\kappa_2(\theta) \ll \kappa_1(\theta) \approx \langle \cos(\theta - \phi) \rangle = \langle \hat{\phi} \cdot \hat{\theta} \rangle, \tag{39}$$

where $\langle x \rangle \equiv x\Theta(x)$, with $\Theta(x)$ being the Heaviside step function. Now, the flow rule results from the substitution of Eqs. (37) and (39) into Eq. (26):

$$d\tilde{\epsilon}^p(\theta) = J(\theta)d\tilde{\sigma} = \frac{\langle \hat{\phi} \cdot d\tilde{\sigma} \rangle}{h}\hat{\psi}. \tag{40}$$

This equation establishes a bilinear relation between the incremental stress and the plastic deformation. This is characterized by an absence of plastic deformation for stress increments such as $\hat{\phi} \cdot d\tilde{\sigma} < 0$ and a plastic deformation, always oriented along the flow direction ψ, for stress increments such as $\hat{\phi} \cdot d\tilde{\sigma} > 0$. At the micromechanical level, this means that the sliding contacts have a well defined response under incremental load: In the case $\hat{\phi} \cdot d\tilde{\sigma} < 0$ the load typically drives them to the elastic regime $|f_t| < \mu f_n$. Otherwise, there is a sliding at each one of these contacts in a direction which does not depend of the direction in the stress space along which the load is applied. This unidirectionality of the plastic deformation is confirmed by several experimental results on plane strain deformation [58] and it is an essential ingredient of the hardening elastoplasticity [43,59]. The fact that this relation is obtained using a simple discrete element model suggests that it is possible to interpret the flow rule of plasticity from the collective response of all sliding contacts.

A. Stress-dilatancy relation

In soil mechanics the plastic flow rule is interpreted in terms of the incremental work done during loading [58]

$$dW = pde + qd\gamma. \tag{41}$$

According to the ***critical state theory***, under large monotonic loads the material reaches a limit state where it behaves purely frictional, deforming isochorically during loading and having constant friction coefficient [58]. Numerical simulations of the biaxial test using polygonal packings seems to

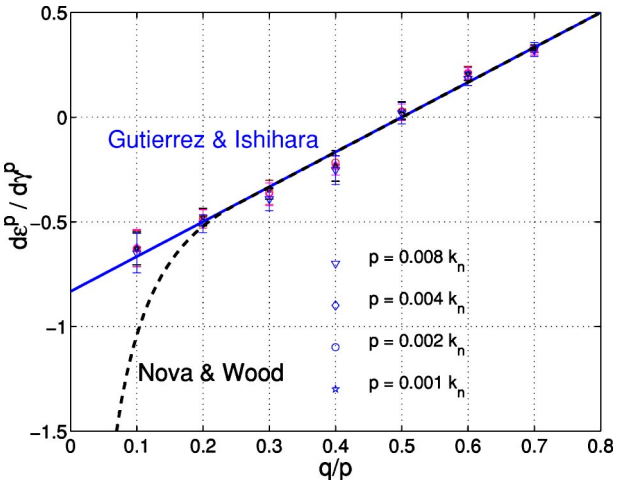

FIG. 13. Dilatancy versus the stress ratio. The solid curve represents a fit with the Gutierrez and Ishihara model. The dashed curve represents the relation given by the Nova and Wood model.

verify this limit condition [29]. As shown in Fig. 3, the granular assembly reaches this critical state, where the volumetric strain as well as the stress ratio keeps approximately constant except for some stress fluctuations, which remain for large deformations. Neglecting those fluctuations, the incremental work done at the critical state can be approximated by

$$dW_c = qd\gamma = M_c p d\gamma, \tag{42}$$

where M_c is the frictional constant at critical state. As far as granular materials are concerned, it is assumed that the deformation is almost completely plastic ($d\tilde{\epsilon} \approx d\tilde{\epsilon}^p$), so that the elastic stored energy is negligible and hence almost all the work is dissipated, i.e., $dW \approx dW_d$.

In classical book of Taylor [60] the basic idea of the *stress-dilatancy* theory is discussed. Based on few data on Ottawa standard sand, Taylor concludes that the dissipated work can be assumed to be constant, independent to the state of loading so that

$$dW_d \approx dW_c. \tag{43}$$

Replacing Taylors hypothesis in Eqs. (41) and (42) and neglecting the elastic energy, we obtain

$$d = \eta - M_c. \tag{44}$$

Here we define $d = -de^p/|d\gamma^p|$ as the dilatancy and $\eta = q/p$ as the stress ratio. As shown in Fig. 13, the dilatancy evaluated from our data does not support the simple rule of Eq. (44), but rather a modification of this expression is required

$$d = c(\eta - M_c), \tag{45}$$

where $M = 0.5$ and $c = 1.7$. According to Eq. (34), the flow direction is therefore given by

$$\cos(\psi) = c(M_c - \eta), \quad 0 \leqslant \psi \leqslant \pi. \tag{46}$$

This linear relation between the dilatancy and the stress ratio has been observed in experimental data in triaxial [61] and biaxial [62] tests on sand. The material constant M_c is interpreted as the stress ratio at the critical state [58]. A physical interpretation of c has been presented by Gutierrez and Ishihara [63]. Their theory is based on the fact that loading induces anisotropy, which in turn involves noncoaxiality, that means that the principal directions of the stress do not coincide with those of the incremental plastic strain tensor. This noncoaxiality implies that the dissipated work expressed as the sum of the products of the stress invariants with the plastic strain invariants, as in Eq. (44), is erroneous. The correct expression should be given in terms of the Cartesian components as $dW_d = \sigma_{ij} d\epsilon^p_{ij}$. A straightforward calculation leads to $dW_d = pde^p + cqd\gamma^p$, where $c = \cos(2\Psi)$, Being Ψ the angle of noncoaxiality. Assuming, as the stress-dilatancy theory, that the dissipated energy remains constant during the loading, we obtain $dW_d = pde^p + cqd\gamma^p = cMpd\gamma^p$. This identity leads to Eq. (45). Note that values of c lower than unity are predicted by this theory. Our biaxial tests simulations However, lead to a value $c = 1.7$. Experimental biaxial tests report on values of c ranging form 0.9 to 1.2 [64]. This range goes also beyond the limits of this theory.

An explanation of this contradiction can be done by exploring the coaxiality and power dissipation during load. According to our simulations, the angle of noncoaxiality is a monotonically decreasing function of the stress ratio. This feature is also observed in experiments on sand [65], proving that c is strictly not a material parameter. Furthermore, the plastic dissipation is a monotonically increasing function of the stress ratio. This implies that the basic assumption of the stress-dilatancy theory, that the incremental power dissipation stays constant, is not applicable to our results. Lets make clear that we are not trying to prove with our simplified model that these theories are wrong. Our results only suggest that in the case of extremely high densities some deviations can be expected. Based on experimental data on dense and loose sand, Li and Dafalias conclude that the void ratio should be integral part of the stress-dilatancy relation [66]. According to Gutierrez and Ishihara, not only the void ratio, but also the also the anisotropy of the sample should be included in this relation. A good alternative would be to introduce the fabric coefficients of the sliding contacts in the description of plasticity. We will explore this approach in the following subsections.

B. Limit of small stress ratios

Further important issues should be addressed in the range of small stress ratios. Here the plastic deformations are much lower than the elastic ones so that the above assumptions leading to the stress-dilatancy relation can not be applied. A modification of this theory for small stress ratio has been presented by Nova and Wood [59]. Their model is based on the assumption that the response of the sample must be isotropic for small deviatoric loads, so that the deviatoric plastic deformation $d\gamma^p$ must vanish in the limit $\eta = q/p \to 0$. In order to satisfy this isotropy condition, Nova and Wood propose that Eq. (45) should be replaced by $d = C/\eta$ for small values of η; the constant C is selected by matching this expression with Eq. (45). Contrary to this assumption, our numerical data fits well to the Eq. (45) for small stress ratio as shown the Fig. 13.

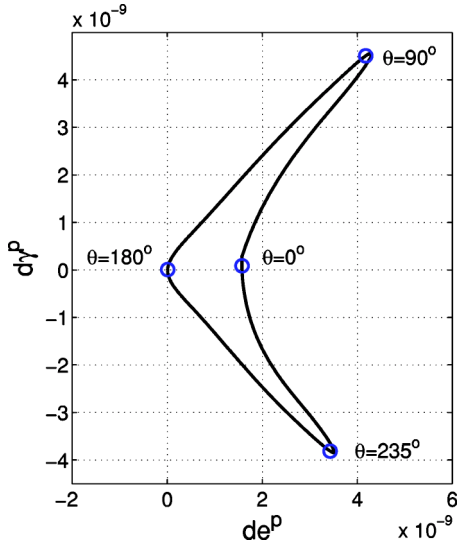

FIG. 14. Plastic envelope response resulting from isotropically compressed samples with a pressure $p=0.001k_n$.

Extrapolating these data to $\eta=0$ brings to light an apparent contradiction: At $q=0$ the contact network is isotropic, so that no deviatoric deformation should appear under isotropic compression. On the other hand, taking $\eta=0$ in Eq. (45) leads to $\psi\neq 0$, which established deviatoric plastic deformation under isotropic loads. To resolve this paradox we plot the plastic part of the strain envelope response when the sample is initially under isotropic pressure, in Fig. 14. We see clearly that the unidirectionality of the plastic deformations breaks down under isotropic condition, so that the flow rule given by Eq. (45) is not valid here. Note from Fig. 14 that further isotropic compression ($\theta=0$) induces only plastic volumetric deformation, which is consistent with the initial isotropy of the polygonal packing. Under extremely small deviatoric loads the isotropy of the assembly is broken, and there is plastic deviatoric deformations with flow direction close to 45°.

This striking effect can be understood from an inspection of the orientational distribution of the sliding contacts. Part (a) of Fig. 6 shows a significant number of contacts reaching the sliding conditions even when the sample is isotropically compressed, The initial distribution of the branch vectors is isotropic. This explains the fact that under isotropic load only volumetric plastic deformations are observed, as shown in Fig. 14.

As shown in Sec. IV B, the subnetwork of sliding contacts departs from isotropy when the sample is subjected to the slightest deviatoric loading. This is because most of the sliding contacts whose branch vector is oriented nearly parallel to the direction of the loading leave the sliding condition. This is represented for $q=0.1p$ in Fig. 7. For low stress ratios, the branch vectors $\vec{\ell}$ of the sliding contacts are oriented nearly perpendicular to the loading direction. Sliding occurs perpendicular to $\vec{\ell}$, so in this case it must be nearly parallel to the loading direction. Then, the plastic deformation must be such that $d\epsilon_3^p \ll d\epsilon_1^p$, so that Eq. (35) yields a flow direction of $\psi\approx 45°$, in agreement with Fig. 14.

Figure 7 shows that by increasing the deviatoric strain results in an increase of the fraction of the sliding contacts.

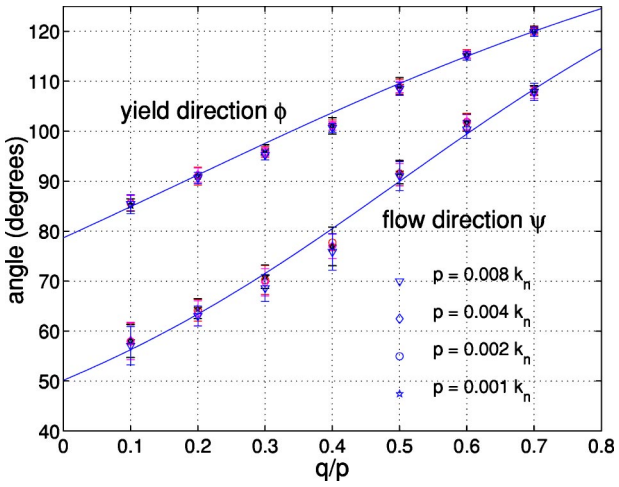

FIG. 15. The flow direction and the yield direction of the plastic response. Solid curves represent a fit using Eqs. (46) and (47).

The average of the orientations of the branch vectors with respect to the load direction decreases with the stress ratio, which in turn results in a change of the orientation of the plastic flow. Close to the failure, some of the sliding contacts whose branch vectors are nearly parallel to the loading direction open, giving rise to a butterfly shape distribution, In this case, the mean value of the orientation of the branch vector with respect to the direction of the loading is around $\varphi=38°$, which means that the sliding between the grains occurs principally around 52° with respect to the vertical. This provides a crude estimate of the ratio between the principal components of the plastic deformation at $q=0.65p$ as $d\epsilon_3^p \approx -d\epsilon_1^p \tan(52°)$. According to Eq. (35) this gives an angle of dilatancy of $\psi\approx 97°$. This crude approximation is reasonably close to the angle of dilatancy of 104° calculated from Eq. (46).

C. Normality condition

The earliest theoretical studies on plasticity came from the study of metals [67]. They were based on the postulation of a yield surface. This surface is supposed to enclose a domain in the stress space where only elastic deformations are possible [1]. The existence of a finite elastic domain leads to the ***normality condition***, which establishes that both plastic flow direction and the yield direction are perpendicular to the yield surface. The question naturally arises as to whether this condition is valid for the plastic deformation of granular materials. Experimentalists on soils say that yield surfaces are difficult to determine because the transition from elastic to elastoplastic behavior is not as sharp as the theory predicts [68]. Loosely speaking, the yield surface appears to be a pragmatic compromise which allows to describe the dependence of plastic deformation on the deformation history, but is not a necessary feature of granular materials [58].

This conclusion becomes clearly apparent if the yield direction and the flow direction are calculated from the plastic part of the strain envelope response using the Eqs. (34) and (35). Both directions are shown in Fig. 15. The results show that they depend only on the stress ratio $\eta=q/p$. The flow

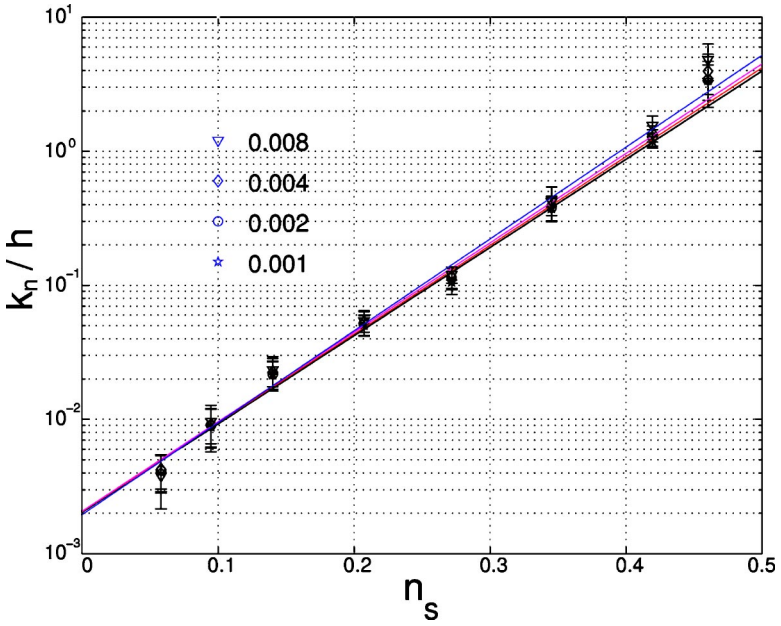

FIG. 16. Inverse hardening modulus h versus fraction of sliding contacts n_s. Different stress values with $q=0.01p, 0.1p, \ldots 0.7p$ and $p/k_n = 0.001$, 0.002, 0.004, and 0.008. The lowest value of n_s corresponds to $q=0.01p$.

direction is fitted by using Eq. (46). The yield direction can be fitted by a similar relation, but with different regression parameters

$$\cot(\phi) = c'(M' - \eta), \quad 0 \leqslant \phi \leqslant \pi. \tag{47}$$

The fitting parameters $M'=0.18$ and $c'=1.1$ do not correspond to the values $M=0.5$ and $c=1.7$ one of the flow direction. This proves that both angles are quite different so that the normality condition is violated. A large amount of experimental evidence has also indicated a clear deviation from the normality condition [68], leading to the so-called nonassociated plasticity [43]. From a micromechanical inspection one can understand this strong deviation from the normality condition. The principal mechanism of plasticity in granular materials is the rearrangement of the grains by sliding at the contacts. This is not the case for microstructural changes in metals, where there is no frictional resistance [69]. Even for small deviatoric loads there is an important fraction of contacts reaching the sliding condition as shown in part (c) of Fig. 6. This is reflected in the strong non-associated behavior shown in Fig. 15 where the yield direction is around 90° and the flow direction around 45°.

The fact that any load involves sliding contacts and its effect on the nonassociated flow rule of plasticity contradicts several constitutive models of granular materials. For example, Nova and Wood establish that due to the absence of sliding contacts at small stress ratios the plastic deformation should be associated like in metals [59]. They introduce a threshold in the stress ratio, above which the onset of frictional contacts breaks the normality rule. This condition is not verified in our simulations, probably due to the fact that in reality not only sliding contacts, but also breaking of grains can occur at low stress ratios at contacts with largest forces [70]. The contribution of grain fragmentation on the plastic deformation is however beyond to the scope of this work.

Loss of contacts seems to play a secondary role in the plastic deformations. The onset of anisotropy of the contact networks at $\eta=0.4$ is probably related to the abrupt change of slope in Fig. 15 around this value.

D. Plastic modulus

In the past two sections we presented a close correlation between the orientational distribution of the sliding contacts and the plastic flow rule. This correlation suggests that plastic deformation of granular materials can be micromechanically described by introducing fabric constants c_i such as in Eq. (28), measuring the anisotropy of the subnetwork of the sliding contacts. This description would be equivalent to the relation between the anisotropy of the contact network and the elastic stiffness tensor presented in Sec. V.

In Sec. IV B we found that the the fraction of sliding contacts is related to the fabric coefficients as $n_s=c_0/a_0$, where c_0 and a_0 are defined by Eqs. (27) and (28). We introduce n_s as an internal variable of the contact network, which will be used to describe the evolution of the plastic modulus with the loading. The plastic modulus h defined in Eq. (36) is related to the incremental plastic strain as $h|d\tilde{\epsilon}^p| \sim |d\tilde{\sigma}|$, which is equivalent to the relation $E_i|d\tilde{\epsilon}^e| \sim |d\tilde{\sigma}|$ between the Young moduli and incremental elastic strain. Thus, just as we related the Young moduli to the average coordination number of the polygons, it is reasonable to connect h to the fraction of sliding contacts n_s. Figure 16 shows that this relation can be fitted to an exponential relation

$$h = h_o \exp(-n_s/n_0), \tag{48}$$

where $h_0=5.0\times10^2 k_n$ and $n_0=0.066$. This exponential dependence contrasts with the linear relation between the Young modulus and the number of contacts obtained in Sec. V. From this comparison, it follows that when the number of contacts is such that $n_s > n_0$, the deformation is not homogeneous, but is principally concentrated more and more around the sliding contacts as their number increases. For low stress

ratios $h \sim 10^2 k_n$ whereas $E_i \sim k_n$ so that plastic deformations, which are inverse proportional to the plastic modulus, are two orders of magnitude smaller than elastic ones. In this case the strain response of the assembly is almost completely elastic. Near to failure we found that $h \sim 10^{-2} k_n$, so that plastic deformations are two orders of magnitude bigger than elastic ones. This corresponds to the well-known rigid-plastic limit for granular materials [4].

VII. CONCLUDING REMARKS

The thrust of this work was the understanding of the effect of induced anisotropy on the elastoplastic response of a polygonal packing in the limit of initially vanishing pore space. The incremental response has been decomposed in an elastic and a plastic part. These components have been correlated to the fabric coefficients, measuring the anisotropy of the contact network and the subnetwork of the sliding contacts.

The incremental elastic response has been described using two Young moduli and two Poisson ratios. Below the stress ratio $q/p < 0.4$, this response can be represented by only one Young modulus and one Poisson ratio, as corresponds to the isotropic elasticity. Above this stress ratio both Young moduli and Poisson ratios are different. These parameters show a linear dependence on the fabric coefficients of the contact network. This result is consistent with several approaches dealing with the connection between the elastic properties of granular materials with the anisotropy of the contact network [32,48,53,56,57]. Our simulations suggest that this correlation could be given by an explicit linear relation between the parameters of the stiffness and the fabric coefficients. We have remarked that the transition to anisotropy around $q/p = 0.4$ is due to the fact that we start with a polygonal packing with zero porosity, where the force distribution is unusually narrow. This is not typical in most granular materials where the force distribution is rather heterogeneous [8]. In dense polygonal packings with finite porosity [29] and disks assemblies, [33,54] small loads open weak contacts and hence induce a smooth transition to the anisotropy for small deviatoric loads. In all cases it is concluded that one can micromechanically characterize the anisotropic elasticity by introducing fabric coefficients, measuring the anisotropy of the contact network.

Another interesting aspect of the incremental response is the unidirectionality of the plastic response, which can be described using a nonassociated flow rule. From numerical simulations of packings of disks, Bardet concluded also that a nonassociated flow rule describes satisfactorily the incremental response [45]. This conclusion is also supported by several experimental tests on plane strain deformation [43,58,59]. Both numerical and experimental results show clearly deviations from the normality condition. This is probably connected to the fact that any load involves sliding contacts so that the elastic regime is vanishing small but not a finite domain as the elastoplasticity establishes [42]. Recent numerical simulations of three dimensional packings of spheres contradict not only the normality postulate [71], but also the unidirectionality of the flow rule [72], leading also to the conclusion that a profound modification of the elastoplasticity theory is required [39].

Apart from the violation of the normality condition, an abrupt anisotropy induced by extremely small deviatoric loads is detected in the subnetwork of the sliding contacts. This results in a breakdown of the unidirectionality of the flow rule at $q=0$, which deserves experimental verifications. This deviation from anisotropy implies deviatoric plastic deformations when the sample is subjected to the smallest deviatoric load. Deviatoric plastic deformation under extremely small deviatoric loads has been also observed in numerical experiments on loose packings of polygons [22] and packings of disks [73], leading to important effects in the mechanical response under cyclic loading [38].

In spite of the complexity of the plastic response, the relation between the dilatancy d and the stress ratio η is given by a simple linear relation $d = c(\eta - M)$. This relation is not only supported by experiments, but also it has been one of the fundamental issues in modeling the stress-strain behavior of soils. Unfortunately the theoretical assumptions of classical models (Taylor [60], Nova and Wood [59], and Gutierrez and Ishihara [63]) are not verified in our model. This leads to the basic question: ***what lies behind of this simple stress-dilatancy relationship?*** Although we cannot give a definitive answer, a physical explanation would be that a granular medium close to the plasticity limit behaves like a *strange fluid*, that obeys this stress-dilatancy relation as an internal kinematical constraint. This constraint becomes apparent near to failure, where plastic deformation dominates, and it could be seen as the counterpart of the well-known incompressibility condition of fluids. This means that for such a *strange fluid* not the mean stress is kinematically undetermined, but that part of the stress which does not work and which corresponds to the component of the stress perpendicular to the (plastic) strain [4]. Thus the usual decomposition of the stress in deviatoric and isotropic part, used in the continuum fluid—and soil-mechanics analyses is not justified [3]. This idea underlies in our opinion the concept of the so-called *mobilized plane* in soil plasticity [74]. The resulting correlation between the mean orientation of the sliding contacts and the plastic flow direction in our calculations suggests that this internal constraint can be micromechanically interpreted from the induced anisotropy of the subnetwork of the sliding contacts.

Since the mechanical response of the granular sample is represented by a collective response of all the contacts, it is expected that the constitutive relation of granular materials can be completely characterized by the inclusion of some internal variables, containing the information about the microstructural arrangements between the grains. We have introduced some internal variables taking into account the anisotropy of the contact force network. The fabric coefficients a_i, measuring the anisotropy of the network of all the contacts, prove to be connected with the anisotropic stiffness. On the other hand, the fabric coefficients c_i, measuring the anisotropy of the sliding contacts, are closely related to the plasticity.

A clear definition of the internal variables is essential to solve the basic paradox of elastoplastic models: The mathematical description of the evolution of a plastic flow rule

with the loading requires the postulation of a finite elastic regime. The existence of this regime implies normality of the flow rule, which contradicts the nonassociated flow rule found in experiments. In our opinion, future work should be oriented towards the elaboration of a theoretical framework connecting the constitutive relation to these internal variables. To provide a complete micromechanically based description of the elastoplastic features, the evolution equations of these internal variables must be included in this formalism. This theory would be an extension of the ideas which have been proposed to introduce the fabric tensor in the constitutive relation of granular materials [11,33,34,53,56,57].

ACKNOWLEDGMENTS

We thank F. Darve, K. Bagi, F. Calvetti, R. Nova, G. Royer-Carfagni, and C. Goldenberg for helpful discussions and acknowledge the support of the *Deutsche Forschungsgemeinschaft* within the research group *Modellierung kohäsiver Reibungsmaterialen* and the European DIGA project HPRN-CT-2002-00220.

APPENDIX: CALCULATION OF THE PARAMETERS OF THE STIFFNESS TENSOR

In this section we present the method used to calculate the Young moduli and the Poisson ratios of the stiffness tensor from the elastic part of the strain envelope response $d\tilde{\epsilon}^e(\theta)$. First we write Eq. (25) as

$$\begin{bmatrix} de^e \\ d\gamma^e \end{bmatrix} = \begin{bmatrix} a_{11} & a_{12} \\ a_{21} & a_{22} \end{bmatrix} \begin{bmatrix} dp \\ dq \end{bmatrix}. \tag{A1}$$

Replacing Eq. (18) into Eq. (23) one obtains that $p = |d\tilde{\sigma}|\cos\theta$ and $q = |d\tilde{\sigma}|\sin\theta$, where θ is the direction of the stress increment. Replacing these equations into Eq. (A1) one obtains

$$de^p = |d\tilde{\sigma}|(a_{11}\cos\theta + a_{12}\sin\theta), \tag{A2}$$

$$d\gamma^p = |d\tilde{\sigma}|(a_{21}\cos\theta + a_{22}\sin\theta), \tag{A3}$$

so that the parameters a_{ij} are evaluated as the Fourier coefficients of de^e and $d\gamma^e$:

$$a_{11} = \frac{1}{\pi|d\tilde{\sigma}|}\int_0^{2\pi} de^e(\theta)\cos\theta d\theta, \tag{A4}$$

$$a_{12} = \frac{1}{\pi|d\tilde{\sigma}|}\int_0^{2\pi} de^e(\theta)\sin\theta d\theta, \tag{A5}$$

$$a_{21} = \frac{1}{\pi|d\tilde{\sigma}|}\int_0^{2\pi} d\gamma^e(\theta)\cos\theta d\theta, \tag{A6}$$

$$a_{22} = \frac{1}{\pi|d\tilde{\sigma}|}\int_0^{2\pi} d\gamma^e(\theta)\sin\theta d\theta. \tag{A7}$$

These equations allow us to calculate the coefficients a_{ij} as a function of the elastic part of the envelope response. The parameter of the stiffness tensor of Eq. (31) are expressed in terms of these coefficients by replacing Eqs. (18) and (21) into Eq. (A1) and comparing the result to Eq. (31). It leads to

$$\frac{1}{E_1} = a_{11} + a_{21} + a_{12} + a_{22}, \tag{A8}$$

$$-\frac{\nu_{12}}{E_2} = a_{11} + a_{21} - a_{12} - a_{22}, \tag{A9}$$

$$-\frac{\nu_{21}}{E_1} = a_{11} - a_{21} + a_{12} - a_{22}, \tag{A10}$$

$$\frac{1}{E_2} = a_{11} - a_{21} - a_{12} + a_{22}. \tag{A11}$$

[1] I. Vardoulakis and J. Sulem, *Bifurcation Analysis in Geomechanics* (Blakie Academic & Professional, London, 1995), Chap. 6.2, pp. 191–196.
[2] G. Gudehus, F. Darve, and I. Vardoulakis, *Constitutive Relations of Soils* (Balkema, Rotterdam, 1984).
[3] I. Vardoulakis, Acta Mech. **49**, 57 (1983).
[4] I. Vardoulakis and J. Sulem, *Bifurcation Analysis in Geomechanics* (Ref. [1]), Chap. 8.1, pp. 281–283.
[5] M. E. Cates, J. P. Wittmer, J.-P. Bouchaud, and P. Claudin, Phys. Rev. Lett. **81**, 1841 (1998).
[6] D. Coppersmith, Phys. Rev. E **53**, 4673 (1996).
[7] J. Geng, D. Howell, E. Longhi, R. P. Behringer, G. Reydellet, L. Vanel, E. Clément, and S. Luding, Phys. Rev. Lett. **87**, 035506 (2001).
[8] F. Radjai, M. Jean, J. J. Moreau, and S. Roux, Phys. Rev. Lett. **77**, 274 (1996).
[9] C. Goldenberg and I. Goldhirsch, Phys. Rev. Lett. **89**, 084302 (2002).
[10] F. Radjai, D. E. Wolf, M. Jean, and J.-J. Moreau, Phys. Rev. Lett. **80**, 61 (1998).
[11] A. Tordesillas, S. D. C. Walsh, and B. S. Gardiner, BIT **44**, 539 (2004).
[12] T. Dietrich, Ph.D. thesis, Universität Karlsruhe, 1976.
[13] I. Vardoulakis and J. Sulem, *Bifurcation Analysis in Geomechanics* (Ref. [1]), Chap. 6.4, pp. 232–237.
[14] P. A. Cundall, Ing.-Arch. **59**, 148 (1989).
[15] I. Vardoulakis, Ing.-Arch. **59**, 106 (1989).
[16] F. Radjai, D. E. Wolf, M. Jean, and J.-J. Moreau, Phys. Rev. Lett. **80**, 61 (1998).
[17] G. Royer-Carfagni and W. Salvatore, Mech. Cohesive-Frict. Mater. **5**, 535 (2000).
[18] F. Kun and H. J. Herrmann, Comput. Methods Appl. Mech. Eng. **138**, 3 (1996).
[19] F. Kun and H. J. Herrmann, Phys. Rev. E **59**, 2623 (1999).

[20] H. J. Tillemans and H. J. Herrmann, Physica A **217**, 261 (1995).
[21] F. Alonso-Marroquin, H. J. Herrmann, and I. Vardoulakis, *Modeling of Cohesive-Frictional Materials* (A. A. Balkema, Leiden, 2004).
[22] F. Alonso-Marroquin and H. J. Herrmann, Phys. Rev. Lett. **92**, 054301 (2004).
[23] G. Royer-Carfagni, *Novel Approaches in Civil Engineering* (Springer-Verlag, Berlin, 2004), pp. 177–185.
[24] C. Moukarzel and H. J. Herrmann, J. Stat. Phys. **68**, 911 (1992).
[25] A. Okabe, B. Boots, and K. Sugihara, *Spatial Tessellations. Concepts and Applications of Voronoi Diagrams*, Wiley Series in Probability and Mathematical Statistics (John Wiley & Sons, Chichester, 1992).
[26] P. A. Cundall and O. D. L. Strack, Geotechnique **29**, 47 (1979).
[27] M. P. Allen and D. J. Tildesley, *Computer Simulation of Liquids* (Oxford University Press, Oxford, 1987).
[28] E. Buckingham, Phys. Rev. **4**, 345 (1914).
[29] A. Pena, A. Lizcano, F. Alonso-Marroquin, and H. J. Herrmann (unpublished).
[30] I. O. Georgopoulus, F. Alonso-Marroquin, I. Vardoulakis, and J. F. Labuz (unpublished).
[31] P. A. Vermeer, Geotechnique **40**, 223 (1990).
[32] M. Madadi, O. Tsoungui, M. Lätzel, and S. Luding, Int. J. Solids Struct. **41**, 2563 (2004).
[33] S. Luding, Int. J. Solids Struct. **41**, 5821 (2004).
[34] S. Luding, *Modeling of Cohesive-Frictional Materials* (A. A. Balkema, Leiden, 2004), pp. 195–206.
[35] S. Luding and H. J. Herrmann, *Bericht Nr. II-7* (Inst. für Mechanik, Universität Stuttgart, 2001), pp. 121–133.
[36] K. Bagi, J. Appl. Mech. **66**, 934 (1999).
[37] K. Bagi, Mech. Mater. **22**, 165 (1996).
[38] F. Alonso-Marroquin, Ph.D. thesis, University of Stuttgart, 2004, Logos Verlag Berlin ISBN 3-8325-0560-1.
[39] F. Darve, E. Flavigny, and M. Meghachou, Int. J. Plast. **11**, 927 (1995).
[40] D. Kolymbas, Arch. Appl. Mech. **61**, 143 (1991).
[41] G. Gudehus, Can. Geotech. J. **20**, 502 (1979).
[42] F. Alonso-Marroquin and H. Herrmann, J. of Eng. Math. (to be published), e-print cond-mat/0403065.
[43] P. A. Vermeer, *Constitutive Relations of Soils* (Balkema, Rotterdam, 1984), pp. 175–197.
[44] H. B. Poorooshasb, I. Holubec, and A. N. Sherbourne, Can. Geotech. J. **4**, 277 (1967).
[45] J. P. Bardet, Int. J. Plast. **10**, 879 (1994).
[46] F. Calvetti, C. Tamagnini, and G. Viggiani, *Numerical Models in Geomechanics* (Swets & Zeitlinger, Lisse, 2002), pp. 3–9.
[47] L. Landau and E. M. Lifshitz, *Theory of Elasticity*, Course of Theoretical Physics Vol. 7 (Pergamon Press, Moscow, 1986).
[48] C. Thornton and D. J. Barnes, Acta Mech. **64**, 45 (1986).
[49] P. A. Cundall, A. Drescher, and O. D. L. Strack, *IUTAM Conference on Deformation and Failure of Granular Materials* (Balkema, Rotterdam, Delft, 1982), pp. 355–370.
[50] S. Luding, R. Tykhoniuk, and A. Thomas, Chem. Eng. Technol. **26**, 1229 (2003).
[51] A. Drescher and G. de Josselin de Jong, J. Mech. Phys. Solids **20**, 337 (1972).
[52] M. Lätzel, S. Luding, H. J. Herrmann, D. W. Howell, and R. P. Behringer, Eur. Phys. J. E **11**, 325 (2003).
[53] M. Lätzel, Ph.D. thesis, Universität Stuttgart, 2002.
[54] C. Goldenberg and I. Goldhirsch, Granular Matter **6**, 97 (2004).
[55] J. R. Ray, Phys. Rev. B **40**, 423 (1989).
[56] R. J. Bathurst and L. Rothenburg, J. Appl. Mech. **55**, 17 (1988).
[57] S. Nemat-Nasser, J. Mech. Phys. Solids **28**, 1541 (2000).
[58] D. M. Wood, *Soil Behaviour and Critical State Soil Mechanics* (ISBN: 0-521-33782-8) (Cambridge University Press, Cambridge, England, 1990).
[59] R. Nova and D. Wood, Int. J. Numer. Analyt. Meth. Geomech. **3**, 277 (1979).
[60] D. W. Taylor, *Fundamentals of Soils Mechanics* (John Wiley, New York, 1948).
[61] P. W. Rowe, Proc. R. Soc. London, Ser. A **269**, 500 (1962).
[62] M. A. Stroud, Ph.D. thesis, University of Cambridge, 1971.
[63] M. Gutierrez and K. Ishihara, Soils Found. **40**, 49 (2000).
[64] R. Lagioia, A. M. Puzrin, and D. M. Potts, Comput. Geotech. **19**, 171 (1996).
[65] I. Vardoulakis and I. O. Georgopoulos, Soils Found. **45** (2), 61 (2005).
[66] X. S. Li and Y. F. Dafalias, Geotechnique **50**, 449 (2000).
[67] D. Drucker and W. Prager, Q. Appl. Math. **10**, 157 (1952).
[68] F. Tatsouka and K. Ishihara, Soils Found. **14**, 63 (1974).
[69] R. Hill, J. Geotech. Eng. **6**, 239 (1958).
[70] G. R. McDowell, M. D. Bolton, and D. Robertson, J. Mech. Phys. Solids **44**, 2079 (1996).
[71] Y. Kishino, Italian Geotechnical Journal **3**, 3 (2003).
[72] F. Calvetti, G. Viggiani, and C. Tamagnini, *Constitutive Modelling and Analysis of Boundary Value Problems in Geotechnical Engineering* (Hevelius Edizioni, Benevento, 2003), pp. 187–216.
[73] R. Garcia-Rojo and H. J. Herrmann, Granular Matter (to be published), e-print cond-mat/0404176.
[74] H. Matsouka, Soils Found. **14**, 47 (1974).